Title

Model observer performance in contrast-enhanced lesions in breast CT: The influence of contrast concentration on detectability.

Journal

Medical Physics, 50(11)

Authors

Lyu, Su Hyun

Hernandez, Andrew

Shakeri, Shadi

et al.

Publication Date

2023-11-01

DOI

10.1002/mp.16667

Peer reviewed

HHS Public Access

Author manuscript

Med Phys. Author manuscript; available in PMC 2024 November 01.

Published in final edited form as:

Med Phys. 2023 November ; 50(11): 6748–6761. doi:10.1002/mp.16667.

Model observer performance in contrast-enhanced lesions in breast CT: The influence of contrast concentration on detectability

Su Hyun Lyu[1,2], **Andrew M. Hernandez**[2], **Shadi Aminololama Shakeri**[2], **Craig K. Abbey**[3], **John M. Boone**[1,2]

[1]Department of Biomedical Engineering, University of California Davis, Davis, CA, 95618, USA

[2]Department of Radiology, University of California Davis, Sacramento, CA, 95817, USA

[3]Department of Psychological and Brain Sciences, UC Santa Barbara, Santa Barbara, CA, 93106 USA

Abstract

Background: The use of iodine-based contrast agent for better delineation of tumors in breast CT (bCT) has been shown to be compelling, similar to the tumor enhancement in contrast-enhanced breast MRI. Contrast-enhanced bCT (CE-bCT) is a relatively new tool, and a structured evaluation of different imaging parameters at play has yet to be conducted. In this investigation, data sets of acquired bCT images from 253 patients imaged at our institution were used in concert with simulated mathematically inserted spherical contrast-enhanced lesions to study the role of contrast enhancement on detectability.

Purpose: To quantitatively evaluate the improvement in lesion detectability due to contrast enhancement across lesion diameter, section thickness, view plane, and breast density using a pre-whitened matched filter (PWMF) model observer.

Methods: The relationship between iodine concentration and Hounsfield units (HU) was measured using spectral modeling. The lesion enhancement from clinical CE-bCT images in 22 patients was evaluated, and the average contrast enhancement (ΔHU) was determined. Mathematically generated spherical mass lesions of varying diameters (1, 3, 5, 9, 11, 15 mm) and contrast enhancement levels (0, 0.25, 0.50, 0.75, 1) were inserted at random locations in 253 actual patient bCT datasets. Images with varying thicknesses (0.4 to 19.8 mm) were generated by slice averaging, and the role of view plane (coronal and axial planes) was studied. A PWMF was used to generate receiver operating characteristic (ROC) curves across parameters of lesion diameter, contrast enhancement, section thickness, view plane, and breast density. The area under the ROC curve (AUC) was used as the primary performance metric, generated from over 90,000 simulated lesions.

Corresponding author: John M. Boone, Ph.D. Department of Radiology, University of California Davis Health, 4860 Y Street, Ellison Building Suite 3100, Sacramento, CA 95817, (916) 735-3158, jmboone@ucdavis.edu.

Conflicts of interest:

Authors (CKA, JMB, AMH, and SAS) are stockholders and paid consultants (CKA, AHM, SAS) for a company (Izotropic Corporation) which is commercializing breast CT.

Results: An average 20% improvement (ΔAUC = 0.1) in lesion detectability due to contrast enhancement was observed across lesion diameter, section thickness, breast density, and view plane. A larger improvement was observed when stratifying patients based on breast density. For patients with VGF ≤ 40%, detection performance improved up to 20% (until AUC → 1), and for patients with denser breasts (VGF > 40%), detection performance improved more drastically, ranging from 20–80% for 1- and 5-mm lesions. For the 1 mm lesion, detection performance raised slightly at the 1.2 mm section thickness before falling off as thickness increased. For larger lesions, detection performance was generally unaffected as section thickness increased up until it reached 5.8 mm, where performance began to decline. Detection performance was higher in the axial plane compared to the coronal plane for smaller lesions and thicker sections.

Conclusions: For emerging diagnostic tools like CE-bCT, it is important to optimize imaging protocols for lesion detection. In this study, we found that intravenous contrast can be used to detect small lesions in dense breasts. Optimal section thickness for detectability has dependencies on breast density and lesion size, therefore, display thickness should be adjusted in real-time using display software. These findings may be useful for the development of CE-bCT as well as other x-ray-based breast imaging modalities.

1. INTRODUCTION

The use of iodine-based contrast agent for better delineation of tumors in breast CT (bCT) has been shown to be compelling [1], similar to the tumor enhancement in contrast-enhanced breast MRI (CE-bMRI) [2] and contrast-enhanced dual-energy digital mammography (CE-DM) [3]. Indeed, the use of intravenous contrast injection in whole body CT applications also adds important diagnostic information to the CT examination. While different organs have different vascular perfusion characteristics which impact the timing of and peak enhancement levels for that organ [4], in the case of solid tumors the “leaky vessel” phenomena resulting from angiogenesis leads to the “wash in” and “wash out” of iodinated contrast agent in the interstitial space surrounding the tumor [5]. This has been called the enhanced permeability and retention (EPR) [6] effect. CE-bMRI and CE-DM also capitalize on the EPR effect, although CE-DM is a 2D imaging modality.

CE-bCT is a relatively new tool, and a structured evaluation of different imaging parameters at play has yet to be conducted. This study aims to examine the independent and co-dependent effects of contrast, breast density, lesion size, view plane, and section thickness on contrast-enhanced lesion detectability, building from previous work on unenhanced lesion detectability [7]. While a clinical trial is the ideal approach for this kind of study, the time, expense, and large database needed to adequately represent the screening population makes this approach challenging and costly. A simulation study is used here in lieu of a clinical study, and we have chosen a hybrid simulation method, in which mathematically generated lesions are inserted into actual patient CT images. This method has been implemented with mammographic backgrounds [8–10] and bCT background [7]. Moreover, a model observer is proposed in lieu of a human observer to evaluate lesion detectability in the simulated images. Mathematical model observers have shown to reasonably predict human observer performance in bCT [11,12] as well as in other breast imaging modalities [8,13,14].

In this investigation, data sets of acquired bCT images from a cohort of patients imaged at our institution were used in concert with simulated mathematically inserted spherical lesions to study the role of contrast injection. To compare performance with previous work, unenhanced simulated lesions were inserted into the acquired breast CT image data using a previously-reported algorithm, and results of a pre-whitened matched filter model observer were compared to previously reported work [7].

The lesion enhancement arising from contrast-enhanced bCT images in 22 patients was evaluated, and the contrast enhancement (average increase in Hounsfield Unit, ΔHU) was characterized. These clinical results were used to compute contrast levels for the simulated lesions, over a range from 0% to 100% contrast enhancement levels. More complex methods have been proposed to simulate clinically-relevant iodinated lesions involving heterogenous enhancement patterns and rim enhancement [15]. Our model does not attempt to simulate intra-lesion heterogeneity, but this simplified approach may be useful in evaluating more general effects of contrast across a range of clinical parameters. The pre-whitened matched filter was used to quantify detection performance using the area under the receiver operating characteristic curve (AUC) as a performance metric. The improvement in detection due to contrast injection was quantified across breast density, lesion size, view plane, and section thickness.

2. METHODS

2.1. Breast CT system and imaging technique

Prototype bCT systems built in our laboratory at UC Davis were used to acquire bCT data sets from patients in an IRB-approved study. The laboratory has developed four generations of bCT scanners as described in Ghazi *et al.* [16]. Image data sets from the first and second generation bCT scanners, which are very similar in design, were used in this study and are briefly described here.

A tungsten anode x-ray tube, collimator, and flat-panel x-ray detector were integrated into a cone-beam bCT scanner and powered by an integrated bearing-motor-encoder system. The gantry rotates in the horizontal plane during acquisition, using an 80 kV x-ray beam with 0.2 mm copper filtration. The flat-panel detector (Varian 4030CB; Varian, Palo Alto, CA) was operated in 2 × 2 binning mode, with a native dexel size of 0.194 mm. The x-ray tube and detector rotated ≥ 360 degrees around the breast to capture 500 cone-beam projection images in about 16 seconds. Image acquisition protocols were not altered for contrast imaging.

A variation of the Feldkamp algorithm [17] was used to reconstruct the projection images. The projection data were reconstructed into a 512 × 512 matrix with an isotropic voxel size of 0.4 mm. Low-frequency cupping artifacts were corrected using a previously-reported polynomial-fitting algorithm [18]. A previously-reported segmentation algorithm [19] was then used to label each voxel in each bCT image as either air, skin, adipose tissue, dense fibroglandular tissue, or sparse fibroglandular tissue, producing segmentation volumes which are perfectly aligned with the gray-scale images.

2.2 Patient Study

A total of 322 women were imaged on our first and second generation bCT scanners as part of several IRB-approved clinical trials. Patients receiving a score of BIRADS 4 or 5 based on their diagnostic breast examination were eligible to enroll in our studies. These patients eventually underwent breast biopsy, and the resulting pathology report was considered ground truth (benign or malignant). In our research imaging protocol, the bCT scan took place just prior to the breast biopsy. For research scans involving contrast, pre- and post-contrast scans were acquired on both breasts. 100 mL of contrast agent (Omnipaque-350; GE Healthcare, Waukesha, WI) [20] was intravenously injected at a rate of 4 mL/sec using a power-injector. Post-contrast scanning in the affected breast began on average 90 seconds after the start of injection.

Most patients received four bCT scans according to contrast imaging protocol, but patients electing not to receive contrast and/or contralateral imaging received one to three scans. Of 913 total scans, 253 pre-contrast scans that were artifact-free, contained the breast in the field of view, and were void of breast implants were selected for this study.

2.3 Relationship between iodine concentration and Hounsfield units

Our study depends upon the assumption that HU and iodine concentration are linearly related [21,22]. This relationship was measured using spectral modeling. The bCT system used to acquire patient data used an 80 kV tube potential with a 0.2 mm copper filter as described in Section 2.1. This spectrum was modeled using the tungsten anode spectral model using interpolating cubic splines (TASMICS) model [23], and a thickness of 140 mm of soft tissue was added to the beam to simulate the attenuation (and beam hardening) of the median breast. The attenuation of 10 mm added thickness of water with various concentrations of iodine (0, 2, 5, 10, 15, 20, 25, 30, 35, 40, 45, 50 mg/mL) was simulated, allowing the estimation of the HU for each iodine concentration. Linear regression was used to compute the relationship between iodine concentration [I] and HU. An R2 value of 1.000 was found. The spectral model demonstrated that [I] (mg/mL) is linearly related to HU. The linear relationship is given in Equation 1:

$$HU = 5.246 \times [I] \tag{1}$$

2.4. Simulation of lesions

2.4.1 Overview: Generation of synthetic lesion images—The methodology for generating synthetic lesion images was described by Packard *et al.* [7] and is summarized here. Mathematically generated lesions were inserted at random locations in patient bCT images with the lesion centers (x, y, z) selected using a random number generator. A check was performed on the surrounding $64 \times 64 \times 64$ voxels to ensure that the inserted lesion was fully contained within the breast parenchyma (adipose and fibroglandular tissue). Synthetic unenhanced lesions were inserted into these subvolumes. The resulting volume with the synthetic lesion, $f_{sim}[i, j, k]$, is shown in Equation 2:

$$f_{sim}[i,j,k] = f[i,j,k] + \left(\Delta\ I \times M(d_{TB}[i,j,k]) \times M\left(\frac{1}{2}D - d_{LC}[i,j,k]\right)\right) \quad (2)$$

where $f[i,j,k]$ is the bCT volume and $\Delta\ I$ is the average difference in HU between adipose and fibroglandular tissue in the bCT image. $M(d_{TB}[i,j,k])$ is the tissue boundary modulation term, ranging from 0–1, which modulates based on $d_{TB}[i,j,k]$, the distance to the nearest tissue boundary from voxel $[i,j,k]$. D is the lesion diameter, $d_{LC}[i,j,k]$ is the distance to the lesion center from voxel $[i,j,k]$, and $M(\frac{1}{2}D - d_{LC}[i,j,k])$ is the lesion boundary modulation term, also ranging from 0 – 1, which blurs the lesion edges based on the distance to the nearest lesion boundary from voxel $[i,j,k]$. Both modulation functions are determined on a patient data set basis by mathematically modeling the edge roll-off at adipose/fibroglandular tissue boundaries to ensure that the resolution of the added lesion matches the resolution of the background bCT image.

After a lesion is inserted into the 3D volume, a $64 \times 64 \times 1$ image of the lesion is generated by either extracting the center slice of the 3D volume for 0.4 mm slice thickness or by slice averaging across multiple adjacent slices.

2.4.2 Synthetic contrast enhancement—It has been observed in unenhanced bCT images that when a lesion infiltrates a region of fibroglandular tissue, it does not change the attenuation coefficient of the native fibroglandular region [7,24]. However, when the unenhanced lesion extends into a region of adipose tissue, it increases the attenuation coefficient of that region to essentially match the intensity of the native fibroglandular tissue. In iodinated contrast imaging, the same process is observed, but the attenuation coefficients of both fibroglandular and adipose regions are further increased to the same value such that the entire lesion is enhanced. Figure 1 displays pre- and post-contrast images for one patient from our study with an enhancing invasive mammary carcinoma, where these phenomena can be observed. These observations inform our methodology for simulating contrast enhancement: after unenhanced lesions are mathematically inserted into breast subvolumes, each voxel within the spherical lesion boundary is enhanced to simulate contrast uptake. While there are BI-RADS lexicons describing enhancing lesions in terms of shape, spiculation, and enhancement pattern, our simple addition of a spherical, uniformly enhancing lesion does not attempt to simulate these clinical features.

The extent to which each lesion is enhanced was investigated. Leaky vasculature resulting from angiogenesis is known to be the primary cause of rapid local enhancement in malignant tumors. We hypothesized that enhancement could also be patient-dependent, and examined potential relationships between contrast enhancement and patient-specific factors. 22 patients from our data set who had biopsy-proven malignant mass lesions and received pre-contrast and post-contrast imaging were studied. For each lesion, contrast enhancement was quantified by computing the increase in HU (ΔHU) in the lesion between the post-contrast and pre-contrast images. The effects of tumor volume, differential glandular intensity (ΔI), and contrast delay, i.e., the time between the start of contrast injection until

post-injection scanning, on ΔHU were investigated. In addition, the effect of patient size in terms of body mass index (BMI) was studied to determine potential dependencies on these parameters.

No notable relationships were found between ΔHU and tumor volume ($R^2 = 0.0253$), ΔI ($R^2 = 0.163$), contrast delay, or BMI ($R^2 = 0.0406$). It was concluded thatΔHU is primarily related to the extent of angiogenesis and the permeability of angiogenetic microvessels in any given tumor. With this observation, the method for enhancing lesions was simplified such that each voxel within the simulated lesion would increase by $\overline{\Delta HU}$, the mean enhancement observed in the 22-patient lesion cohort. The mean enhancement $\overline{\Delta HU}$ was found to be 76.0, and the standard deviation σ was 33.5. The equivalent iodine concentrations based on Equation 1 are 14.5 mg/cm^3 and 6.39 mg/cm^3, respectively.

The resulting equation for simulating contrast-enhanced lesions is shown in Equation 3:

$$f_{sim}[i,j,k] = f[i,j,k] + \left((\Delta I \times M(d_{TB}[i,j,k])) + (\alpha \times \overline{\Delta HU})\right) \times M\left(D/2 - d_{LC}[i,j,k]\right) \quad (3)$$

where $\overline{\Delta HU}$, the mean enhancement observed in the clinical data set of malignant lesions and α is a scaling term to study the effect of different amounts of contrast on lesion detectability. Five different values of α were studied: 0, 0.25, 0.50, 0.75, 1. The corresponding HUs are 0, 19.0, 38.0, 57.0, and 76.0, respectively, and the equivalent iodine concentrations in mg/cm^3 are: 0.0, 3.6, 7.2, 10.9, and 14.5, respectively. In addition to contrast level, the effects of lesion diameter, section thickness, breast density, and view plane on lesion detectability were also studied. Six different lesion diameters (1, 3, 5, 9, 11, 15 mm) and six different section thicknesses (0.4, 1.2, 1.9, 3.5, 5.8, 19.8 mm) were used. The selected lesion diameters represent the size range of mass lesions found over 322 clinical breast CT images. Microcalcifications were not simulated for this study. Data sets spanning a broad range of known breast densities were used to address the role of breast density. Breast density was quantified in terms of the volumetric glandular fraction (VGF), which is defined as:

$$VGF = \frac{n_g}{n_g + n_a} \quad (4)$$

where n_g represents the number of fibroglandular voxels and n_a represents the number of adipose voxels in the segmentation volume of the breast. VGF was computed for each patient and then categorized into one of six bins (0–10%, 11–20%, 21–30%, 31–40%, 41–50%, >50%). 2D images were generated from the coronal and axial view planes to study the role of view plane. The range of parameters studied herein is summarized in Table 1.

Examples of inserted non-contrast (α = 0) and contrast-enhanced (α = 1) lesions are shown in Figure 2. In the added lesion columns, a black voxel signifies 0 HU was added to that region, a gray voxel signifies Δ I HU was added to that region, and a white voxel signifies

$\Delta I + (\alpha \times \overline{\Delta HU})$ was added to that region. As described in Equation 3, each computed voxel was additionally modulated by M depending on its distance to the nearest adipose/glandular tissue boundary and to the nearest lesion boundary to ensure smoothness of edges.

2.5. Model observer for detectability evaluation

In the ideal scenario, human observers (e.g., expert breast imaging radiologists) would be used evaluate the detectability of simulated lesions. Given that we study the independent and codependent effects of the parameters listed in Table 1 across 253 patient data sets, at least 91,080 simulated lesion images would need to be evaluated, making a human observer study infeasible. Accordingly, a pre-whitened matched filter (PWMF) [8,25], a mathematical observer, was used to evaluate the detectability of simulated lesions in a signal known exactly (SKE), location known exactly (LKE) detection study. The PWMF is considered the ideal observer under the assumption of a stationary Gaussian image background and has been shown to outperform human observers in bCT images [26]. In an SKE/LKE task, the shape of the signal is known, and the location of the lesion is known exactly, and the PWMF makes use of the signal profile and image power spectrum to compute a decision variable which is used to evaluate detectability. Packard *et al.* also utilized a PWMF in lieu of human observers to evaluate detectability of simulated *unenhanced* lesions across clinically relevant parameters in previous work [7]. While the PWMF may not be perfectly accurate with respect to human observers, its *relative* performance is considered reliable in this comparative analysis across clinically relevant parameters.

To implement the PWMF, the mean signal profile and the power spectrum of the image background must first be computed. For each bCT volume data set, for a given combination of contrast level, lesion diameter, section thickness, and view plane, N viable lesion centers are first found, which are used to compute N $64 \times 64 \times 1$ lesion-present patches and N $64 \times 64 \times 1$ lesion-absent patches. A patch generated with an added lesion is denoted as $I_n^+(x, y)$ and a patch generated at the same lesion center without an added lesion is denoted as $I_n^-(x, y)$, where n represents the n^{th} lesion. The mean signal across the N lesion-present and N lesion-absent patches is denoted as $\overline{I^+}(x, y)$ and $\overline{I^-}(x, y)$, respectively, and the mean signal profile between them is defined as:

$$\bar{S}(x, y) = \overline{I^+}(x, y) - \overline{I^-}(x, y) \tag{5}$$

$\Delta\, I_n^-(x, y)$ is defined by:

$$\Delta I_n^-(x, y) = H[x, y] \times \left(I_n^-[x, y] - \overline{I^-}[x, y]\right) \tag{6}$$

where $H[x, y]$ is defined as the inner product of two 1-D Hamming filters [27] and serves to mitigate artifacts arising from the cyclic nature of the discrete Fourier transform by attenuating the difference as it approaches the edge of the image [25,28]. $I_n^-[x, y]$represents the

lesion-absent patch at the n^{th} lesion, and $\bar{I}^{-}[x, y]$ represents the average of all lesion-absent patches.

The mean noise power spectrum in Fourier space is computed from the lesion-absent patches as follows:

$$\bar{PS}(f_x, f_y) = \frac{1}{N-1} \sum_{n=1}^{N} \left| \Delta \widehat{I_n^-}(x, y) \right|^2 \tag{7}$$

where $N - 1$ represents the loss of one degree of freedom since $\Delta I_n^-(x, y)$ involves a subtraction, and the caret represents the 2D Fourier transform. By characterizing the frequency dependence of the anatomical background in Equation 7, dividing by this frequency dependence flattens the resulting frequency dependence, which is the "whitening" part of the PWMF observer.

The PWMF in the spatial domain is then defined as:

$$w[x, y] = FT^{-1}\left\{ \frac{FT\{\bar{S}(x, y)\}}{\bar{PS}(f_x, f_y) + R} \right\} \tag{8}$$

where FT represents the 2D Fourier transform, FT^{-1} represents the 2D inverse Fourier transform, and R is a regularization constant used to mitigate high frequency noise in the filter. R was empirically determined to be 10^6. Figure 3 shows the mean signal $\bar{S}(x, y)$, the 2D PWMF, and a surface-contoured plot of the PWMF for a 15 mm lesion. We observe that the PWMF weights intensities at the lesion boundary.

2.6. PWMF performance evaluation

The PWMF was then used to detect lesions in a separate set of simulated bCT image patches as a signal known exactly, location known exactly detection task. The PWMF was applied to each patch to compute a scalar valued decision variable λ_n. For each bCT volume data set, N unique viable lesion centers were first generated using a random number generator. For each lesion center and combination of parameters, a lesion-present patch $I_n^+[x, y]$ was generated by the lesion insertion process. For that lesion center, the decision variable λ_n is the sum of the pixel intensity of the image patch $I_n[x, y]$ weighted by the PWMF, $w[x, y]$:

$$\lambda_n = \Sigma_{x,y} I_n[x, y] \times w[x, y] \tag{9}$$

N additional unique lesion centers were then found and used to compute N lesion-absent decision variables using Equation 9. Independent lesion centers were generated between the sets of lesion-present and lesion-absent patches so as not to correlate the decision variables. The decision variables were plotted on a histogram as depicted in Figure 4 and converted

to an empirical receiver operating characteristic (ROC) curve [29] by plotting sensitivity and false positive rate over a range of detection thresholds. For each ROC curve, the area under the ROC curve (AUC) was computed, where the AUC characterizes the detectability performance of that combination of parameters on that specific patient bCT image. To get an estimate of the overall detectability related to a combination of parameters, the individual AUCs were averaged over the K image volumes (K = 253). The standard deviation of AUCs was also computed.

2.7. Statistical analysis

Performance estimates were plotted with 95% confidence error bars in Section 3, which are given by the following equation:

$$CI_{95} = \overline{AUC} \pm 1.96 \times \frac{\sigma}{\sqrt{K}} \tag{10}$$

where CI_{95} is the 95% confidence interval, $\overline{AUC}$ is the mean AUC across all bCT images, σ is the standard deviation of AUCs across all bCT images, and K is the number of image volumes. Confidence intervals are plotted to represent uncertainty in the plots.

In Section 3, the improvement in average detectability performance, $\Delta\overline{AUC}$, is computed between detectability estimates in contrast-enhanced ($\alpha = 1$)and unenhanced plots ($\alpha = 0$) using Equation 11:

$$\Delta\overline{AUC} = \overline{AUC}_{contrast-enhanced} - \overline{AUC}_{unenhanced} \tag{11}$$

The percent increase is then calculated using Equation 12, recognizing that detection performance is 0% when $AUC = 0.5$, and detection performance is 100% when $AUC = 1.0$.

$$\%\ increase\ = 100 \times \frac{\Delta\overline{AUC}}{0.5} \tag{12}$$

The percent increase serves as a metric of improvement using contrast enhancement and is used to observe trends in the study across clinical parameters. For all comparative tests, a non-parametric approach is taken using the Mann-Whitney U-test. Statistical significance is defined as a difference with $p < .05$. When multiple comparisons are made, a Bonferroni correction was applied by dividing the desired significance (0.05) by the number of comparisons. All tests were two-sided. Statistical analyses were performed in MATLAB (MATLAB; TheMathWorks Inc., Natick, MA).

2.8. Number of inserted lesions, N

N is the number of lesions used to compute the mean signal profile in Equation 5, the mean noise power spectrum in Equation 7, and the PWMF response histogram for each image. Packard *et al.* used $N = 500$.

Due to the computationally expensive process of lesion simulation, the feasibility of reducing N was investigated. Detectability estimates for 1- and 5- mm unenhanced lesions in the thinnest section were generated for $N = 10$, 25, 50, 100, 200, 300, 400, and 500. Each detectability estimate (AUC) was repeated ten times to infer error. Two-sided Student's t-tests were used to determine whether differences in detectability estimates using different N's were statistically significant. Mean AUCs were plotted as a function of the number of inserted lesions, N, in Figure 5.

For both 1- and 5-mm lesions, it was found that when N is less than 100, there is notable fluctuation and larger error when estimating AUC. As N increases, error steadily decreases, and AUC estimates begin to converge. Based on Figure 5, we determined that reducing N to 200 could be used to reduce computational time but still provide an accurate estimation of detectability with high precision. The differences in performance estimates using $N = 500$ and $N = 200$ were not statistically significant ($p = .117$, $p = .351$ for 1- and 5-mm lesions, respectively).

3. RESULTS

3.1. Model Validation

Detection performance for unenhanced lesions was plotted against similar results from Packard *et al.* in Figure 6. Performance estimates for 1-, 5-, and 15-mm diameter lesions averaged over all breast densities are plotted as a function of section thickness. Notably, our results are of the axial view plane only, while Packard *et al.*'s results are averaged over three views planes: coronal, axial, and sagittal. There were differences between the projection planes that likely explain the differences between the two data sets. Moreover, our data set contained 253 image volumes, and Packard utilized 151 image volumes. Considering the differences between the studies being compared, there is reasonable agreement between trends observed in this study and Packard *et al.*'s.

3.2. Effects of contrast enhancement

Detection performance was averaged across all breast densities (i.e., VGFs) and both view planes and plotted as a function of contrast level (α) for three lesion sizes in Figure 7. As expected, contrast injection improved detection performance for all lesion sizes (1 mm: $p < .01$; 5 mm: $p < .01$; 15 mm: $p < .01$). For the 1 mm lesion, detection performance steadily improved by 20% from $AUC = 0.85$ with no contrast enhancement ($\alpha = 0$) to $AUC = 0.95$ at full contrast enhancement ($\alpha = 1$).

3.3. Effects of section thickness

Detection performance was averaged across all breast densities (i.e., VGFs) and both view planes and plotted as a function of section thickness for six lesion sizes in Figure 8. Figure

8a displays performance estimates for unenhanced lesions ($\alpha = 0$). The thinnest section (0.4 mm) may not be the ideal section thickness for unenhanced lesion detection. For the 1 mm lesion, detection performance rises to a mild peak around 1.2 mm thickness as section thickness increases before falling off more rapidly. For larger lesions, detection performance is generally unaffected as section thickness increases up until thickness reaches 5.8 mm, where performance begins to decrease.

Figure 8b displays performance estimates for contrast-enhanced lesions ($\alpha = 1$). Detection performance improves for contrast-enhanced lesions across all section thicknesses and lesion sizes (family-wise $p < .01$). With contrast, detection improves approximately 5–20% until maximum detection performance (i.e., AUC = 1) is reached. When section thickness is less than 2 mm, the AUC estimate for contrast-enhanced lesions greater than 1 mm in diameter is approximately 1.0.

3.4. Effects of lesion size

Detection performance was averaged across all breast densities (i.e., VGFs) and both view planes and plotted as a function of lesion diameter for a thin section (0.4 mm) and a thick section (19.8 mm) in Figure 9. As might be expected, larger lesions are uniformly easier to detect than smaller lesions in both thin and thick sections. Detection performance improves for contrast-enhanced lesions across lesion size and section thickness (family-wise $p < .01$). When contrast is used, detection performance improves up to 20% (until AUC $\rightarrow$ 1) across lesion diameter for both thin and thick sections.

3.5. Effects of breast density

The distribution of patient breast densities from our patient data set is shown in Table 2.—A small fraction of patients (3/253 patients, 1.2%) had primarily fatty breasts (VGF ≤ 10%), and a small fraction of patients (10/253 patients, 3.9%) had very dense breasts (VGF > 50%). The remaining patients (240/253 patients, 94.9%) had low to moderately dense breasts ranging from 11–50% glandularity. Detection performance was averaged across all section thicknesses and both view planes and plotted as a function of VGF for three lesion sizes.

Effects of breast density on detection performance can be observed in Figure 10. Figure 11 displays improvement in detectability with contrast injection in terms of $\Delta\ AUC$ and percent increase. For patients with VGF ≤ 40%, detection performance improves up to 20% (until AUC 1), and for patients with denser breasts (VGF > 40%), detection performance improves more drastically, ranging from 20–80% for 1- and 5-mm lesions. There is no statistically significant difference in detection performance for a 1 mm lesion in a fatty breast with and without contrast (VGF ≤ 10%; $p = 0.4$). For every other breast density category, the improvement in detection performance for the 1 mm lesion with and without contrast is statistically significant (11–20%: $p < .01$; 21–30%: $p < .01$; 31–40%: $p < .01$; 41–50%: $p < .01$; >50%: $p < .01$).

3.6 Effects of view plane

Effects of view plane on lesion detectability can be observed in Figure 12. Detection performance was averaged across all breast densities (i.e., VGFs) and plotted as a function of section thickness for 1- and 5-mm lesions viewed in the coronal and axial planes.

Equivalent or greater detection performance is achieved using the axial view compared to the coronal view for all section thicknesses, both lesion sizes, and with and without contrast. For the 1 mm unenhanced lesion, there is no statistically significant difference in detection performance between axial and coronal views using 0.4 mm section thickness ($p = 0.61$). For thicker sections, the axial view outperforms the coronal view (z = 1.2 mm: $p < .01$; z = 1.9 mm: $p < .01$; z = 3.5 mm: $p < .01$; z = 5.8 mm: $p < .01$; z = 19.8 mm: $p < .01$). For the 5 mm unenhanced lesion, there is no statistically significant difference in detection performance between axial and coronal views using section thicknesses of 0.4 mm ($p = 0.45$), 1.2 mm ($p = 0.54$), 1.9 mm ($p = 0.65$), and 3.5 mm ($p = 0.15$). The axial view outperforms the coronal view at thicker sections (z = 5.8 mm: $p < .01$; z = 19.8 mm: $p < .01$). Contrast injection improves detection performance approximately 20% ($\Delta\ AUC = 0.1$) for both lesion sizes across all section thicknesses.

4. DISCUSSION

We sought to quantify improvement in lesion detectability due to contrast enhancement across lesion diameter, section thickness, breast density, and view plane. Figure 7 shows the effect of contrast level on lesion detectability. At full contrast ($\alpha = 1$), detection performance improves up to 20% (until AUC 1) from unenhanced detection performance. Similar improvement is also observed when visually comparing unenhanced and contrast-enhanced plots in Figures 8, 9, and 12. A larger improvement in detection performance is observed in Figure 11 when stratifying patients based on breast density. In unenhanced bCT, we observe that lesion detectability has dependencies on patient breast density. The AUC for unenhanced lesions in patients with mostly fatty breasts (VGF < 20%) exceeds 0.9, while the AUC for unenhanced lesions in patients with very dense breasts (VGF > 50%) ranges from 0.55 – 0.70. With contrast, AUC exceeds 0.9 for all lesion sizes across all breast densities. In effect, when using injected contrast, lesion detectability becomes only slightly dependent on breast density.

Section thickness is an important factor when displaying tomographic images, but not the only one. Image acquisition and reconstruction methods, kernel size in filtered backprojection, and reconstructed voxel size also matter, and the tradeoff between image resolution and image noise is well known. Therefore, it is hard to determine a universal optimal section thickness for displaying bCT. Aside from very thin sections, detection performance generally decreases as section thickness increases, as might be expected. Thicker sections often suffer from superposition of fibroglandular anatomy which can obscure lesions and reduce detectability. This is the primary limitation of 2D projection imaging modalities such as mammography or tomosynthesis. Reduced detectability is more pronounced in denser breasts compared to fatty breasts since more fibroglandular tissue is superimposed [7], therefore, optimal section thickness is also dependent on breast density.

For this reason, we have built our in-house bCT viewer to enable the reader to adjust the display slice thickness in all three projections simultaneously in real-time. For the general bCT system, a middle ground between selecting an overly thin slice at the cost of quantum noise and an overly thick slice at the cost of anatomical noise should be found. Intravenous contrast appears to improve detection performance around 20% on average and may compensate for losses in detection performance due to selecting an overly thin or overly thick section.

In Section 3.6 it was determined that equivalent or greater detection performance is achieved using the axial plane compared to the coronal plane across clinical parameters. In a previous study, Packard *et al.* demonstrated that the sagittal view performed very similarly to the axial view, which is expected as the breast is approximately radially symmetrical along the anterior-posterior line. For this reason, we only evaluated the two view planes and averaged other parameters across these two view planes. In our validation study in Section 3.1, there are differences between Packard's performance estimates and ours, although both curves take on similar trends. The improved detection performance for the 1 mm lesion in our study may be due to advanced image reconstruction techniques [16] that were used in this study but not in Packard *et al.*'s study. These techniques enabled sharper image resolution which in turn improved the added lesion resolution, since the added lesion boundaries were blurred to match the resolution of the patient image. The improved resolution appears to be more impactful when detecting smaller lesions, i.e., 1 mm lesions. Another likely reason for these differences is the differences in patient data sets since Packard used a 151-patient data set, and a 253-patient data set was used in this study. Despite the axial view performing better for lesion detection, bCT images are traditionally viewed in the coronal plane, or with all three orthogonal views on the same display. In clinical practice, radiologists tend to view bCT images in thin sections, therefore, differences in detectability between the two views are likely to be minor.

This study had limitations. The patient images used to generate hybrid images contained pre-contrast images of the affected breast. It is possible that some lesion-absent ROIs contained real mass lesions, but these instances were likely few given the small relative size of a mass lesion compared to the volume of a breast in pendant position. Furthermore, AUC was averaged over 400 ROIs across 253 images, therefore, any bias introduced by individual ROIs containing mass lesions was likely mitigated by averaging procedures. Breast cancer presents as both masses and microcalcifications, but only mass lesions were simulated in this study. Partial volume effects appear to influence lesion detectability as mass lesions become very small. In this study, partial volume was modeled using a single modulation function, M, independent of lesion size. It is possible that this function may have been insufficient to fully model partial volume effects for the 1 mm diameter lesion. Only malignant masses from our clinical CE-bCT data set were studied for enhancement calibration, but benign masses are known to minimally enhance as well [1]. The methodology for adding contrast was simplified in this study such that each voxel within the inserted lesion was uniformly enhanced. In clinical images, enhancing lesions can appear more visibly heterogenous, particularly for lesions containing microinvasions of ductal carcinoma in situ (DCIS), cysts, or distortions. Furthermore, a simple SKE/LKE detection task was implemented such that

the PWMF fixed the signal profile and did not take lesion shape into consideration. Lesion phenotypes that are known to indicate malignancy, e.g., spiculations, were not simulated in this study. Furthermore, despite the simplifications of fixing an SKE signal, it has been shown that the PWMF models optimal detection performance and is similar to human detection performance [26]. For the purpose of modeling human observers, it appears that the PWMF model is useful.

5. CONCLUSION

Contrast enhancement was simulated for synthetic spherical lesions, and enhancement levels were calibrated based on 22 malignant masses from our clinical CE-bCT data set. In this model observer study, the improvement in detection due to contrast injection was quantified across breast density, lesion size, view plane, and section thickness. Small lesions are generally harder to detect in dense breasts, but these results suggest that injected contrast can substantially improve detection performance in dense breasts. Optimal section thickness for detectability has dependencies on breast density and lesion size, therefore, display thickness should be adjusted in real-time using display software.

For emerging diagnostic tools like CE-bCT, it is important to optimize imaging protocols for lesion detection. These findings are not only useful for the optimization and development of CE-bCT but may also be relevant in other x-ray-based breast imaging modalities such as contrast-enhanced breast tomosynthesis [30] and dual energy contrast-enhanced mammography [31].

Acknowledgements:

This research was supported in part by NIH grants R01 CA181081 and R01 EB025829

REFERENCES

1. Prionas ND, Lindfors KK, Ray S, et al. Contrast-enhanced Dedicated Breast CT: Initial Clinical Experience1. Radiology. 2010;256(3):714–723. doi:10.1148/radiol.10092311 [PubMed: 20720067]
2. Morris EA. Breast cancer imaging with MRI. Radiol Clin North Am. 2002;40(3):443–466. doi:10.1016/s0033-8389(01)00005-7 [PubMed: 12117186]
3. Jochelson MS, Dershaw DD, Sung JS, et al. Bilateral Contrast-enhanced Dual-Energy Digital Mammography: Feasibility and Comparison with Conventional Digital Mammography and MR Imaging in Women with Known Breast Carcinoma. Radiology. 2013;266(3):743–751. doi:10.1148/radiol.12121084 [PubMed: 23220903]
4. Curry FRE, Adamson RH. Vascular permeability modulation at the cell, microvessel, or whole organ level: towards closing gaps in our knowledge. Cardiovasc Res. 2010;87(2):218–229. doi:10.1093/cvr/cvq115 [PubMed: 20418473]
5. Miles KA. Tumour angiogenesis and its relation to contrast enhancement on computed tomography: a review. Eur J Radiol. 1999;30(3):198–205. doi:10.1016/S0720-048X(99)00012-1 [PubMed: 10452718]
6. Maeda H The enhanced permeability and retention (EPR) effect in tumor vasculature: the key role of tumor-selective macromolecular drug targeting. Adv Enzyme Regul. 2001;41(1):189–207. doi:10.1016/S0065-2571(00)00013-3 [PubMed: 11384745]
7. Packard NJ, Abbey CK, Yang K, Boone JM. Effect of slice thickness on detectability in breast CT using a prewhitened matched filter and simulated mass lesions. Med Phys. 2012;39(4):1818–1830. doi:10.1118/1.3692176 [PubMed: 22482604]

8. Burgess AE, Jacobson FL, Judy PF. Human observer detection experiments with mammograms and power-law noise. Med Phys. 2001;28(4):419–437. doi:10.1118/1.1355308 [PubMed: 11339738]
9. Timberg P, Båth M, Andersson I, Mattsson S, Tingberg A, Ruschin M. In-plane visibility of lesions using breast tomosynthesis and digital mammography: In-plane visibility of lesions using BT and DM. Med Phys. 2010;37(11):5618–5626. doi:10.1118/1.3488899 [PubMed: 21158273]
10. Shaheen E, De Keyzer F, Bosmans H, Dance DR, Young KC, Ongeval CV. The simulation of 3D mass models in 2D digital mammography and breast tomosynthesis: Simulation of 3D mass models. Med Phys. 2014;41(8Part1):081913. doi:10.1118/1.4890590
11. Chen L, Boone JM, Abbey CK, et al. Simulated lesion, human observer performance comparison between thin-section dedicated breast CT images versus computed thick-section simulated projection images of the breast. Phys Med Biol. 2015;60(8):3347–3358. doi:10.1088/0031-9155/60/8/3347 [PubMed: 25825980]
12. Han M, Kim B, Baek J. Human and model observer performance for lesion detection in breast cone beam CT images with the FDK reconstruction. Sidky E, ed. PLOS ONE. 2018;13(3):e0194408. doi:10.1371/journal.pone.0194408
13. Eckstein MP, Abbey CK, Whiting JS. Human vs model observers in anatomic backgrounds. In: Kundel HL, ed. ; 1998:16–26. doi:10.1117/12.306180
14. Carton AK, de Carvalho PM, Li Z, Dromain C, Muller S. Assessment of mass detection performance in contrast enhanced digital mammography. In: Mello-Thoms CR, Kupinski MA, eds. ; 2015:941608. doi:10.1117/12.2081772
15. de la Rosa RS, Carton AK, de Carvalho PM, Li Z, Muller S, Bloch I. Preliminary study of CEDBT and CESM performances using simulated analytical contrast uptakes. In: 2018 IEEE 15th International Symposium on Biomedical Imaging (ISBI 2018). IEEE; 2018:792–795. doi:10.1109/ISBI.2018.8363691
16. Gazi PM, Yang K, Burkett GW, Aminololama-Shakeri S, Anthony Seibert J, Boone JM. Evolution of spatial resolution in breast CT at UC Davis. Med Phys. 2015;42(4):1973–1981. doi:10.1118/1.4915079 [PubMed: 25832088]
17. Feldkamp LA, Davis LC, Kress JW. Practical cone-beam algorithm. J Opt Soc Am A. 1984;1(6):612. doi:10.1364/JOSAA.1.000612
18. Ghazi P, Hernandez AM, Abbey C, Yang K, Boone JM. Shading artifact correction in breast CT using an interleaved deep learning segmentation and maximum-likelihood polynomial fitting approach. Med Phys. 2019;46(8):3414–3430. doi:10.1002/mp.13599 [PubMed: 31102462]
19. Packard N, Boone JM. Glandular segmentation of cone beam breast CT volume images. In: Medical Imaging 2007: Physics of Medical Imaging. Vol 6510. SPIE; 2007:1091–1098. doi:10.1117/12.713911
20. Omnipaque. Accessed September 25, 2022. https://www.gehealthcare.com/products/contrast-media/omnipaque
21. Wang L, Liu B, Wu XW, et al. Correlation between CT attenuation value and iodine concentration in vitro: discrepancy between gemstone spectral imaging on single-source dual-energy CT and traditional polychromatic X-ray imaging. J Med Imaging Radiat Oncol. 2012;56(4):379–383. doi:10.1111/j.1754-9485.2012.02379.x [PubMed: 22883644]
22. Ehn S, Sellerer T, Muenzel D, et al. Assessment of quantification accuracy and image quality of a full-body dual-layer spectral CT system. J Appl Clin Med Phys. 2017;19(1):204–217. doi:10.1002/acm2.12243 [PubMed: 29266724]
23. Hernandez AM, Boone JM. Tungsten anode spectral model using interpolating cubic splines: Unfiltered x-ray spectra from 20 kV to 640 kV. Med Phys. 2014;41(4):042101. doi:10.1118/1.4866216
24. Johns PC, Yaffe MJ. X-ray characterisation of normal and neoplastic breast tissues. Phys Med Biol. 1987;32(6):675–695. doi:10.1088/0031-9155/32/6/002 [PubMed: 3039542]
25. Burgess AE, Judy PF. Signal detection in power-law noise: effect of spectrum exponents. JOSA A. 2007;24(12):B52–B60. doi:10.1364/JOSAA.24.000B52 [PubMed: 18059914]
26. Chen L, Abbey CK, Boone JM. Association between power law coefficients of the anatomical noise power spectrum and lesion detectability in breast imaging modalities. Phys Med Biol. 2013;58(6):1663–1681. doi:10.1088/0031-9155/58/6/1663 [PubMed: 23422272]

27. Kaiser J, Hamming R. Sharpening the response of a symmetric nonrecursive filter by multiple use of the same filter. IEEE Trans Acoust Speech Signal Process. 1977;25(5):415–422. doi:10.1109/TASSP.1977.1162980

28. Bendat JS and Piersol AG, Random Data: Analysis and Measurement Procedures. John Wiley & Sons, 2011, ch. 11, pp. 366–374.

29. Burgess AE. Comparison of receiver operating characteristic and forced choice observer performance measurement methods. Med Phys. 1995;22(5):643–655. doi:10.1118/1.597576 [PubMed: 7643805]

30. Chong A, Weinstein SP, McDonald ES, Conant EF. Digital Breast Tomosynthesis: Concepts and Clinical Practice. Radiology. 2019;292(1):1–14. doi:10.1148/radiol.2019180760 [PubMed: 31084476]

31. Lewin JM, Isaacs PK, Vance V, Larke FJ. Dual-energy contrast-enhanced digital subtraction mammography: feasibility. Radiology. 2003;229(1):261–268. doi:10.1148/radiol.2291021276 [PubMed: 12888621]

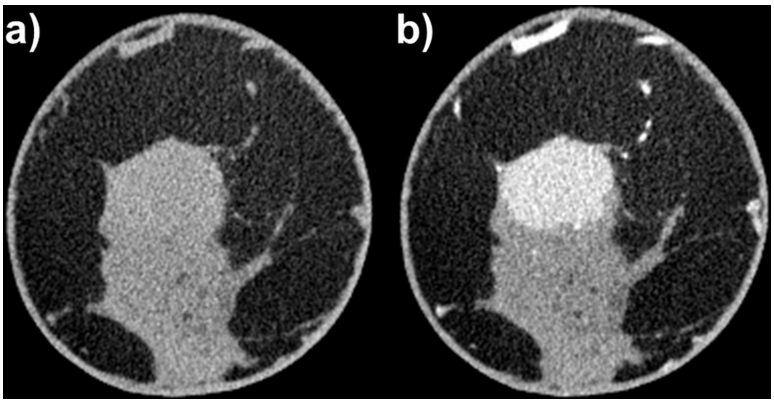

Figure 1.
Pre-contrast (a) and post-contrast (b) coronal bCT images of invasive mammary carcinoma. Local enhancement is visible in the post-contrast image.

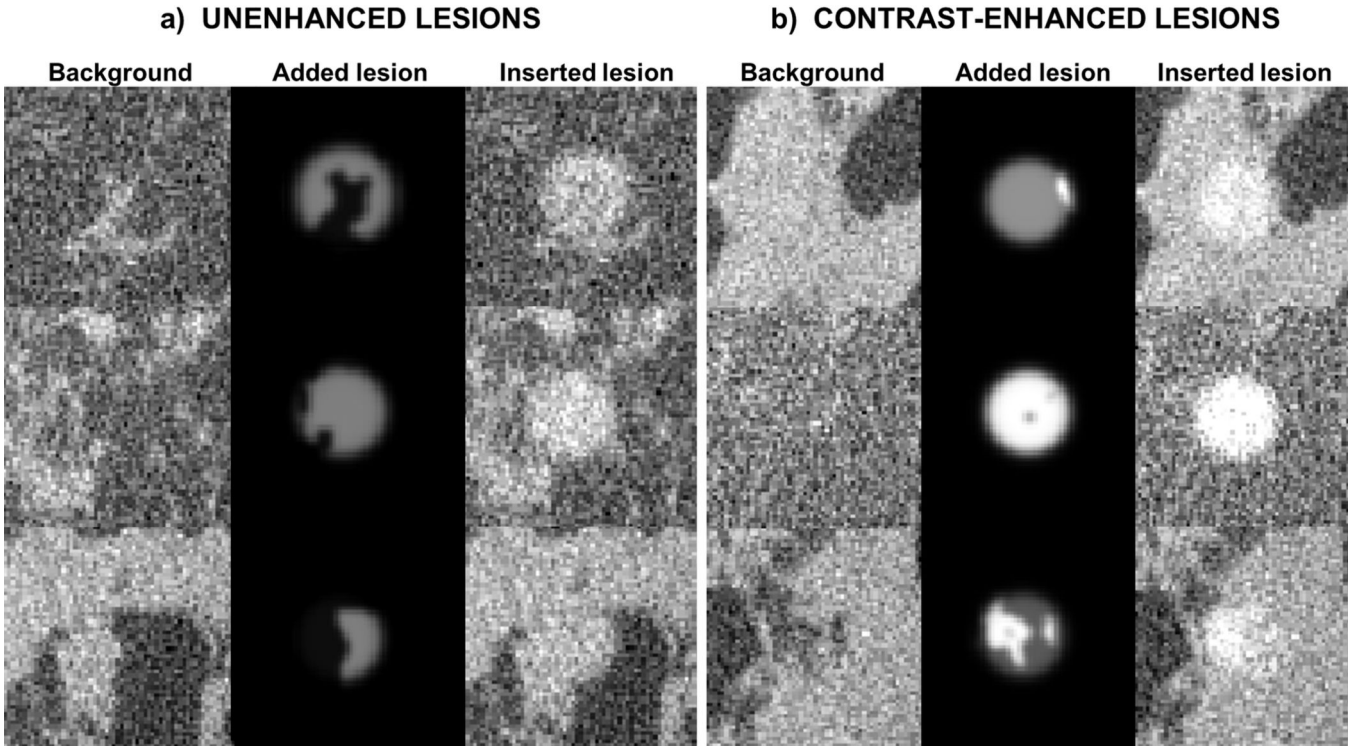

Figure 2.

Example image patches of (a) simulated unenhanced lesions in breast background and (b) simulated contrast-enhanced lesions in breast background. In unenhanced lesions, intensity is only added to adipose regions. In contrast-enhanced lesions, intensity is added to both adipose and fibroglandular regions, with more intensity being added to adipose regions.

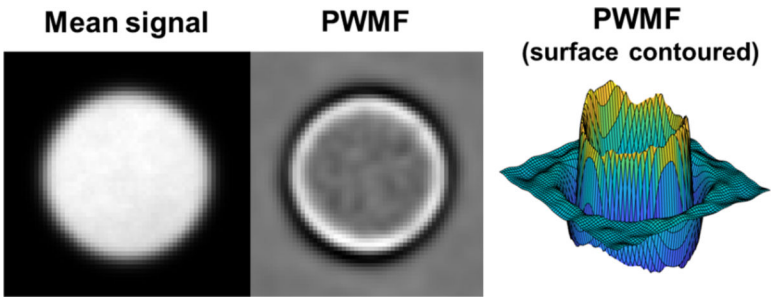

Figure 3.

Computation of PWMF. The leftmost column shows the mean signal of *N* inserted 15 mm unenhanced lesions. The center column shows the 2D PWMF for the same lesion size. A surface contoured plot of the PWMF is shown in the rightmost column. The PWMF emphasizes detection at the lesion boundary.

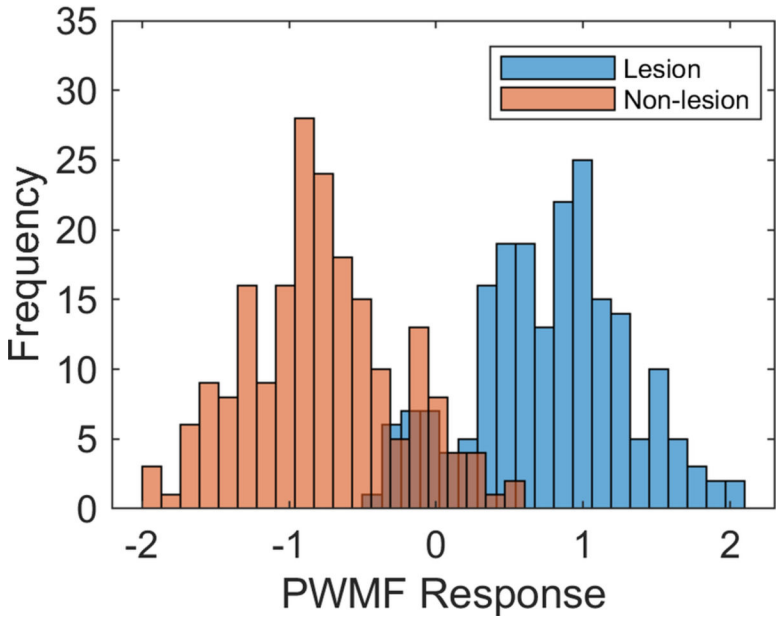

Figure 4.

Example PWMF response histogram for one breast. PWMF responses (i.e., decision variables) are computed and distinguished between input patches with lesions ("Lesion") and without lesions ("Non-lesion"). Responses are used to generate the ROC curve, which can be used to compute the AUC.

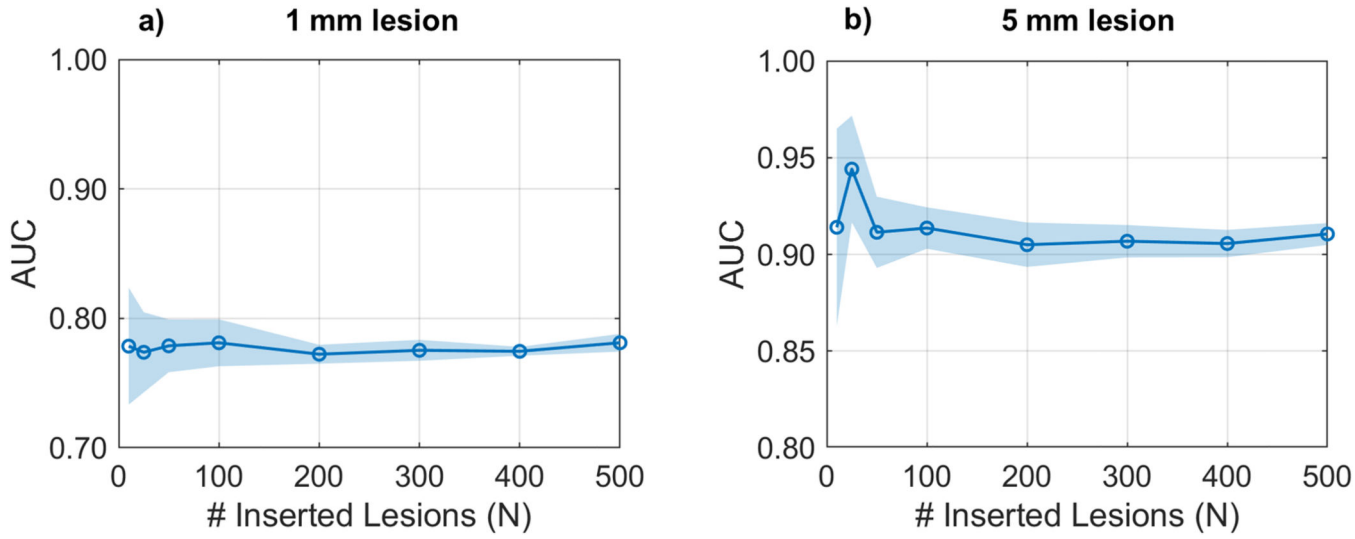

Figure 5.

Effect of number of inserted lesions, *N*, on AUC estimation for (a) 1 mm lesion and (b) 5 mm lesion. Detectability estimates were repeated ten times for $N = 25$, 50, 100, 200, 300, 400, and 500. The mean AUC was plotted for each *N*. Shaded regions correspond to 95% confidence interval for each estimate.

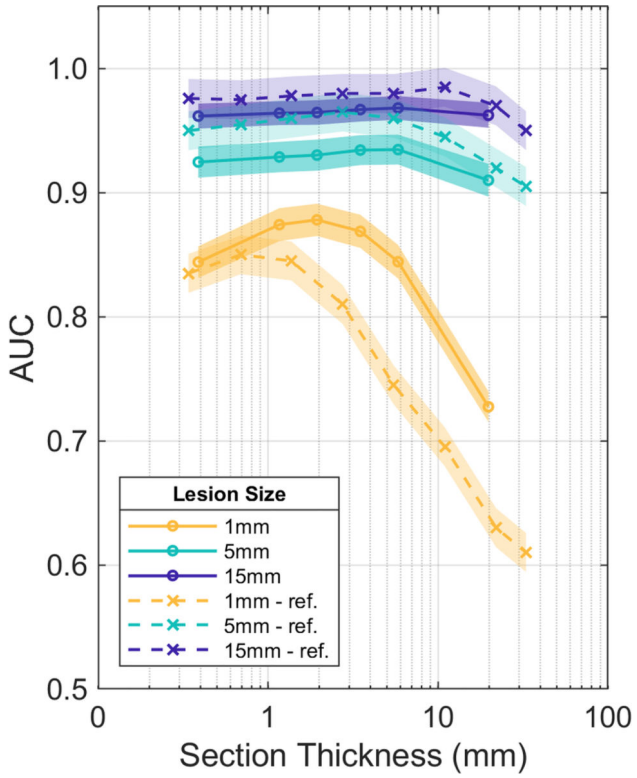

Figure 6.

Model validation. AUC is plotted as a function of section thickness for 1-, 5-, and 15-mm lesions in the axial view plane. Results from this study are compared with results from the reference study (Packard *et al).* Shaded regions correspond to 95% confidence interval for each estimate.

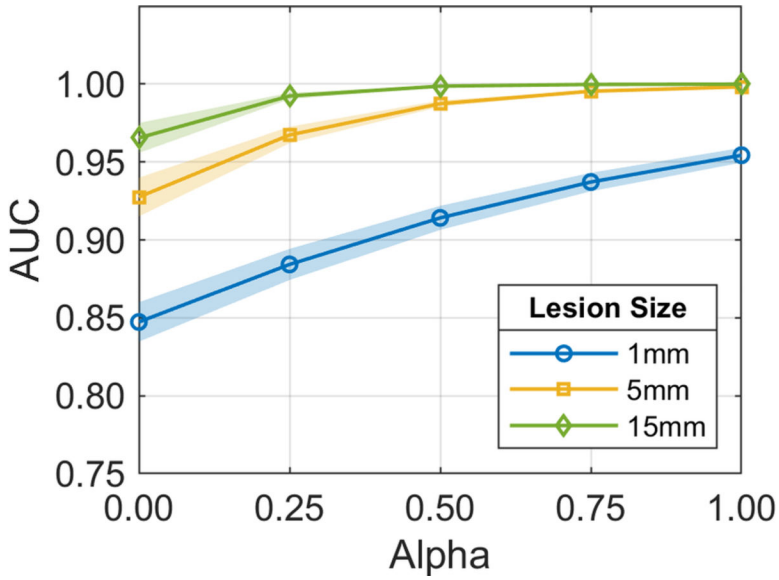

Figure 7.

Effect of contrast levels. AUC is plotted as a function of contrast level α for 1-, 5-, and 15-mm lesion sizes. Shaded regions correspond to 95% confidence interval for each estimate.

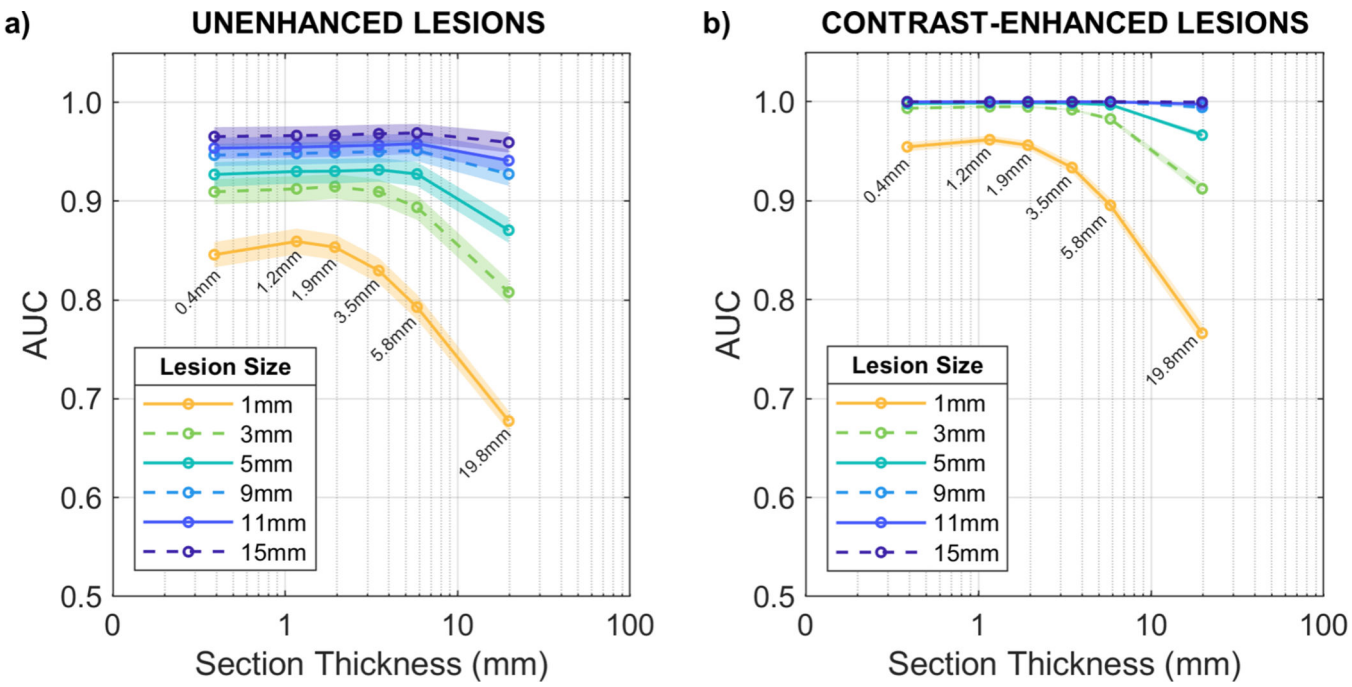

Figure 8.

Effects of section thickness in (a) unenhanced lesion detection and (b) contrast-enhanced lesion detection for six lesion sizes. Shaded regions correspond to 95% confidence interval for each estimate.

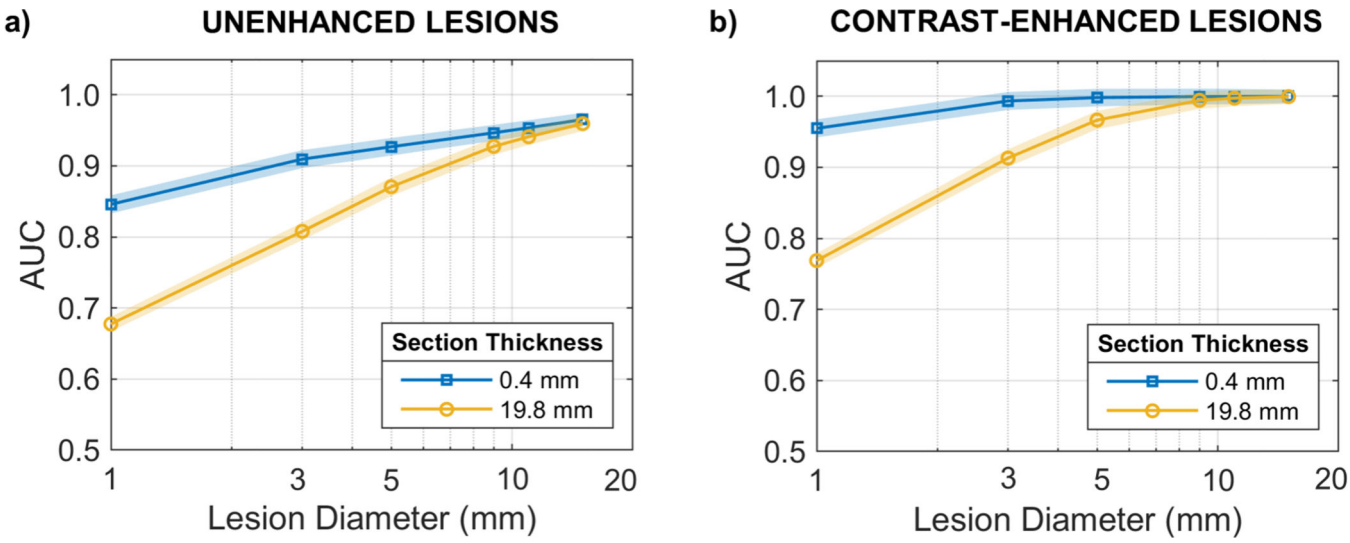

Figure 9.

Effects of lesion size. (a) Performance estimates for unenhanced lesions ($\alpha = 0$) in the thinnest (0.4 mm) and thickest sections (19.8 mm). (b) Performance estimates for contrast-enhanced lesions ($\alpha = 1$) for the thinnest (0.4 mm) and thickest (19.8 mm) sections. Shaded regions correspond to 95% confidence interval for each estimate.

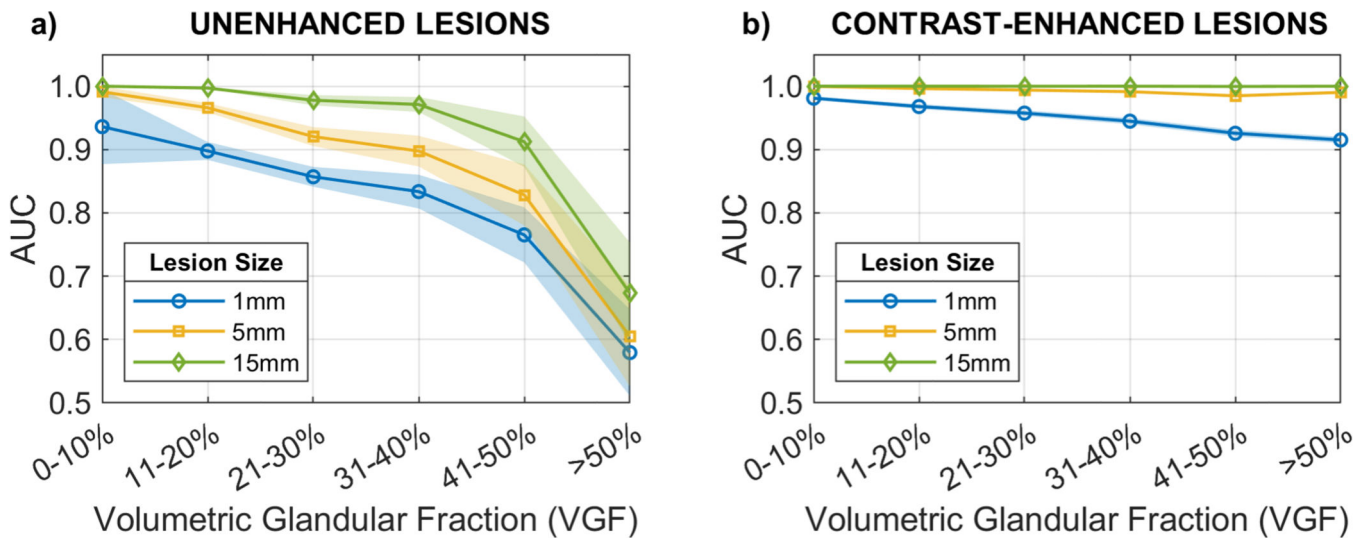

Figure 10.

Effects of breast density. (a) Performance estimates for unenhanced lesions ($\alpha = 0$) for three lesion sizes. (b) Performance estimates for contrast-enhanced lesions ($\alpha = 1$) for three lesion sizes. Shaded regions correspond to 95% confidence interval for each estimate.

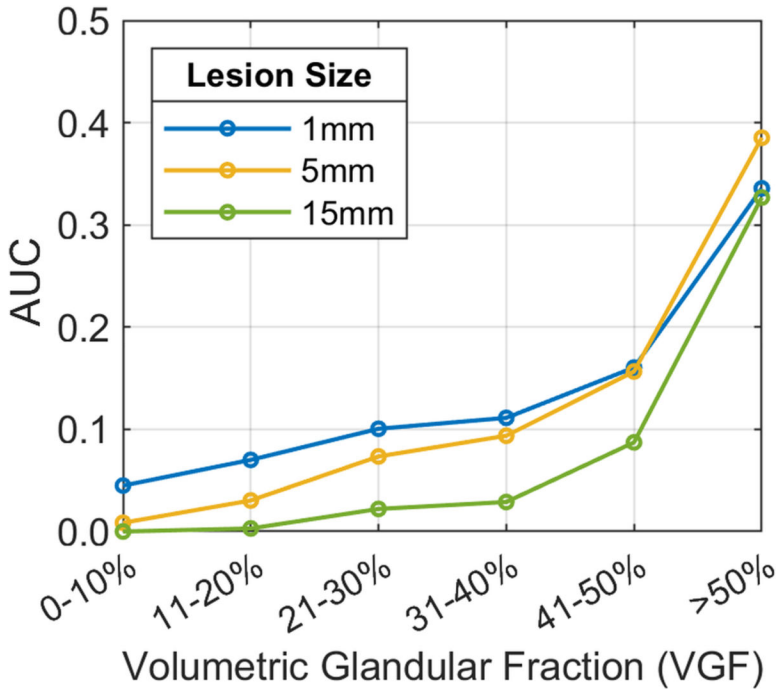

Figure 11.

Improvement in detectability ($\Delta\ AUC$) between contrast-enhanced lesions and unenhanced lesions for three lesion sizes as a function of VGF. Equivalent percent increase is denoted on the right vertical axis.

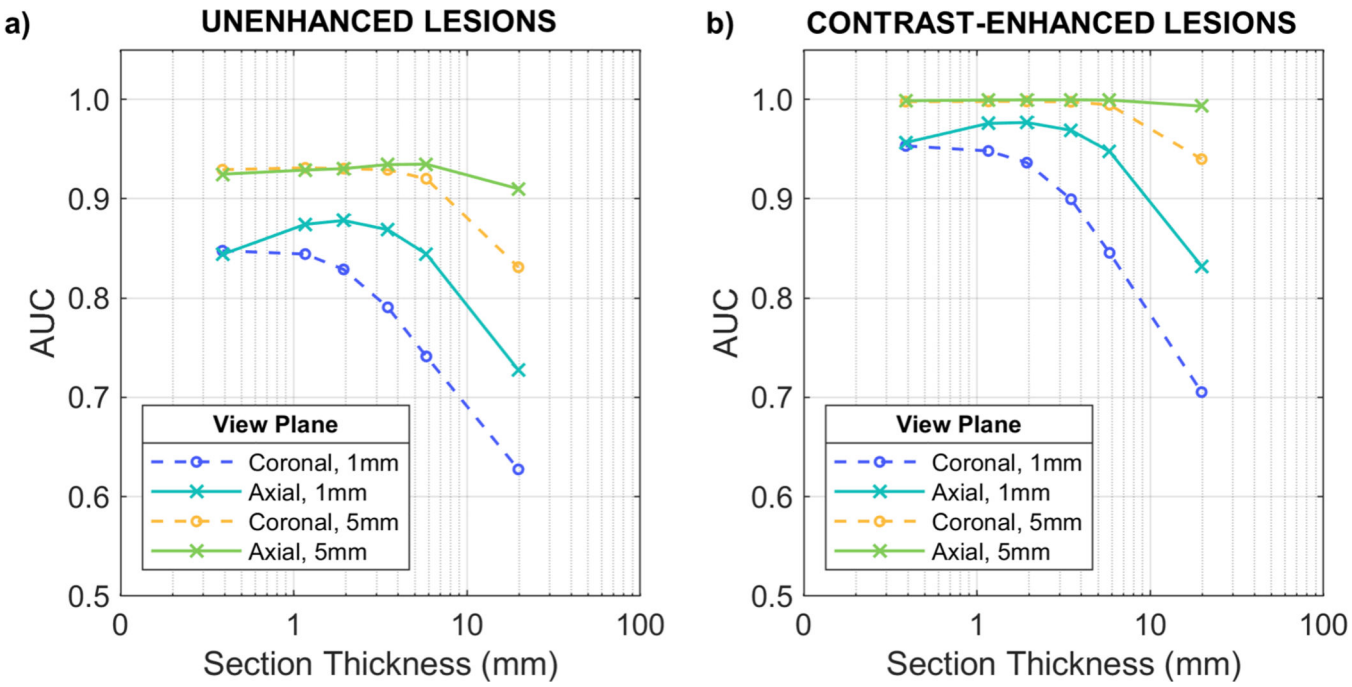

Figure 12.

Effects of view plane on lesion detectability. (a) Detection performance for unenhanced 1 mm and 5 mm lesions ($\alpha = 0$) viewed in coronal and axial planes. (b) Detection performance for 1 mm and 5 mm contrast-enhanced lesions ($\alpha = 1$) viewed in coronal and axial planes.

Table 1.

Range of each parameter studied: alpha (equivalent iodine concentration listed in italics), lesion diameter, section thickness, and view plane.

Alpha	*Equivalent [I] (mg/cm^3)*	Lesion Diameter (mm)	Section Thickness (mm)	Plane
0.00	*0.0*	1	0.4	Coronal
0.25	*3.6*	3	1.2	Axial
0.50	*7.2*	5	1.9	
0.75	*10.9*	9	3.5	
1.00	*14.5*	11	5.8	
		15	19.8	

Table 2:

Distribution of breast densities from patient data set, represented by volumetric glandular fraction (VGF).

VGF	0–10%	11–20%	21–30%	31–40%	41–50%	>50%
N	3	70	104	48	18	10